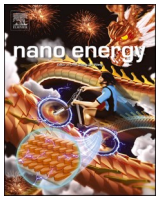
Nano Energy 130 (2024) 110124



Contents lists available at ScienceDirect

Nano Energy

journal homepage: www.elsevier.com/locate/nanoen





# Auxetic kirigami structure-based self-powered strain sensor with customizable performance using machine learning

Jimin Gu [a,b], Yongsu Jung [a], Junseong Ahn [c], Jihyeon Ahn [a], Jungrak Choi [d], Byeongmin Kang [a], Yongrok Jeong [e], Ji-Hwan Ha [a], Taehwan Kim [a], Young Jung [f], Jaeho Park [a], Jiyoung Jung [b], Seunghwa Ryu [a], Ikjin Lee [a], Inkyu Park [a,*]

[a] Department of Mechanical Engineering, Korea Advanced Institute of Science and Technology (KAIST), Daejeon 34141, Republic of Korea
[b] Department of Mechanical Engineering, University of California, Berkeley, CA 94720, USA
[c] Department of Electro-Mechanical Systems Engineering, Korea University, Sejong 30019, Republic of Korea
[d] Electronics and Telecommunications Research Institute (ETRI), Daejeon 34129, Republic of Korea
[e] Korea Atomic Energy Research Institute (KAERI) 11, Daedeok-daero 989 beon-gil, Yuseong-gu, Daejeon 34057, Republic of Korea
[f] Major of Mechanical Engineering, Pukyong National University (PKNU), 45 Yongso-ro, Nam-gu, Busan 48513, Republic of Korea

ARTICLE INFO

*Keywords:*
Self-powered sensor
Strain sensor
Auxetic structure
Machine learning
Customizable performance
AR wearable system

ABSTRACT

Recently, soft material based wearable sensors have discovered numerous applications in healthcare, sports monitoring, and virtual reality/augmented reality (VR/AR) systems. For these sensors, fulfilling user-specified requirements rather than just improving the sensor performance has become an important issue. In this study, a self-powered piezo-transmittance type strain sensor based on auxetic structures was optimized for configurable and user-specified characteristics using a machine-learning surrogate model. The sensor mechanism is based on the optical transmittance change induced by the gap opening of the auxetic kirigami structure. The sensor performance was analyzed according to the geometric design variables, and the optimal design was determined using Bayesian and Gaussian process to maximize the sensor performance for different purposes. The optimally designed geometries were used for self-powered sensors on a structural health monitoring (SHM) system, a human motion monitoring (HMM) system for monitoring sports performance and incorporated into an AR system.

## 1. Introduction

Soft sensors, which are employed as wearable sensors based on soft material compliance, have numerous applications in healthcare [1–4], sports monitoring [5–7], and virtual reality/augmented reality (VR/AR) systems [8–10]. Their flexibility and stretchability make them ideal for use with soft and expandable targets. Additionally, IoT systems field increasingly requires sustainable low-powered or self-powered systems [11–18]. In this context, the need for self-powered sensors has become essential. Solar cells have been developed as an alternative energy source, with the significance of green energy already widely recognized and commercialized, making it a prime example of sustainable energy generation. Among the variety of soft strain sensor types, piezo-transmittance type strain sensors based on the optical transmittance change of the structure, have attracted considerable attention because of their utility in developing self-powered sensor integrated by solar cell, as well as their negligible hysteresis, small drift, high reliability, and high stability [12,19,20]. It offers a powerful advantage: it can be used as a self-powered strain sensor with environmental light unlike the traditionally well-studied types of strain sensors are based on piezo-resistive, piezo-capacitive, and optical polymer-based waveguide structures, which have their own limitations. Piezo-resistive type sensors can exhibit stability and reliability issues [21–26], while piezo-capacitive type sensors have limited sensitivity due to their working mechanism [27–32]. Additionally, optical waveguide type strain sensors require an additional optic-coupler system for peak analysis [33–37]. On the other hand, the piezo-transmittance type strain sensor offers a promising solution for self-powered sensors, aligning with the increasing demand for sustainable and low powered IoT systems.

Nowadays, the specific requirements of a soft sensor can vary widely depending on the application, necessitating a customizable design. In

* Corresponding author.
*E-mail address:* inkyu@kaist.ac.kr (I. Park).

https://doi.org/10.1016/j.nanoen.2024.110124
Received 29 June 2024; Received in revised form 7 August 2024; Accepted 14 August 2024
Available online 15 August 2024
2211-2855/© 2024 Published by Elsevier Ltd.

this regard, user-specified sensor characteristics for a particular application are becoming more important [38] such as the sensor performance optimization with multi-compliance range. Conventional sensors often require modifications to the inherent properties of sensing materials to alter their responses, leading to a trial-and-error fabrication procedure that lacks precise control. Therefore, there is a growing demand for automatic design approaches that can customize sensor characteristics to fit various applications. Especially in the case of self-powered piezo-transmittance type strain sensors, the use of auxetic kirigami structure to achieve precise control over gap opening mechanism brings the benefit of ensuring sensor reliability characteristics, including uniformity and designability [39]. Kirigami structures, rationally designed and cut, allow us to maintain strict control over the gap opening area as well as the stress concentration distribution on overall geometry that are critical to the sensor's performance. This level of control is challenging to achieve if the working mechanism relies on material-driven random cracks. Moreover, by employing these auxetic kirigami structures, there is a potential for developing automatic design approach for user-specified sensing performance optimization.

In this background, we developed a user-designated sensor performance optimization by multi-objective optimization approach that considers sensor sensitivity and compliance in self-powered piezo-transmittance type strain sensor. Our approach applies Bayesian optimization to precisely forecast and adjust sensor characteristics according to user-specified parameters. The use of auxetic kirigami structures ensures a uniform and predictable sensor response, demonstrating the customizable nature of our method. This study introduces a systematic, customizable approach, marking a critical shift towards enabling users to tailor self-powered strain sensor functionality to their unique demands and various applications. This adaptability and customization potential represent a novel contribution, setting our findings apart from existing research. These advancements underscore the transformative potential of our approach, positioning it as a pioneering solution in the field of customizable, self-powered strain sensors.

As shown in Fig. 1, a piezo-transmittance type strain sensor measures strain through the change in light transmittance of a film due to external strain. The proposed sensor has piezo-transmittance characteristics based on the gap-opening mechanism of the kirigami structure with a cellular auxetic pattern composed of unit cells. Among various auxetic structures, rotating rectangular, chiral, and re-entrance structures were selected to obtain the optimum design, since they are typical unit-cell based auxetic structures and can be fabricated as line-based kirigami structures [40–48]. We calculated the sensor response and compliance over the design domain using the finite element method (FEM) to build initial sample for machine learning based surrogate model. Multi-objective Bayesian Optimization (BO) was conducted to maximize the sensitivity or compliance. The BO has high sampling efficiency because it can focus on sampling in the candidate group rather than random design space [49]. Using this process, we customized the sensor design for optimal performance for each different purpose. The sensor design characterization was validated by experimental results. The samples with optimal designs were fabricated by cutting black-pigment-mixed polydimethylsiloxane (BM-PDMS) with a fiber laser. The sensitivity and compliance of the fabricated sensor were compared with those of a simulated model. Various strain sensor structures were employed for distinct applications, such as utilizing a structural health monitoring (SHM) system to monitor rigid and expandable structures, a wearable human motion monitoring (HMM) system, and an augmented reality (AR) system to showcase a wireless wearable system.

## 2. Results

### 2.1. Influential factors in optimization

The sensitivity and compliance of sensor were evaluated for the sensor design optimization. An auxetic kirigami structure-based strain sensor measures changes in light transmittance based on the gap opening of the auxetic structure in response to external strain. The sensitivity of the sensor, expressed as a gauge factor, is calculated as the proportion

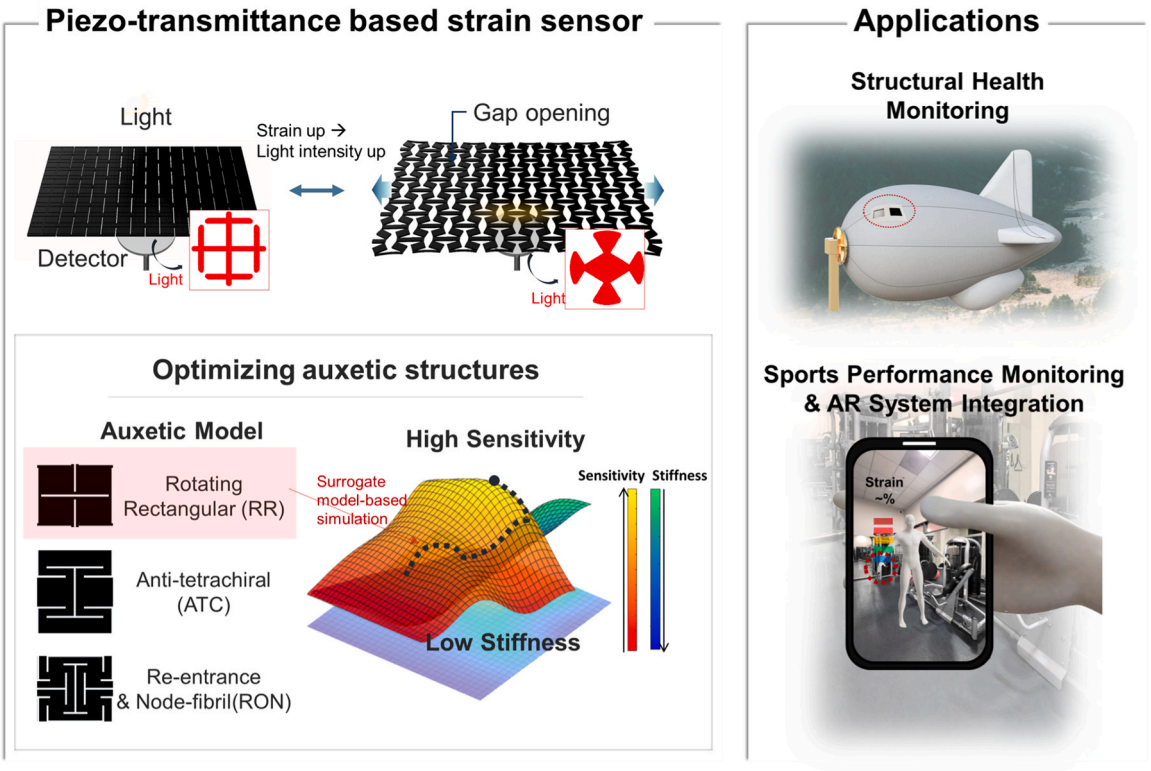



**Fig. 1.** Overall schematic of optimization and customization of the piezo-transmittance soft strain sensor and its applications.

of light intensity change ($I-I_0$) to the initial light intensity ($I_0$):

$$GF = \left[\frac{I - I_0}{I_0}\right] \Big/ \left[\frac{L - L_0}{L_0}\right]$$

Where L is the length of the sample when the strain is applied, and $L_0$ is the initial length of the sample. The relationship with the light intensity and the light transmittance of the sample is further explained in Supporting Information, "Relationship between light intensity and light transmittance." According to this equation, the sensitivity is dependent on the initial light transmittance. The sensor compliance is the reciprocal of the stiffness. We evaluated and referred the sensor compliance by the reaction force needed to stretch the structure. We refer to sensor compliance as the reaction force, and thus minimization of the reaction force is equivalent to maximization of the compliance of the structure. The sizes of a unit cell and cut slit determine the initial light transmittance and the reaction force of the final structure. Three types of auxetic design were employed, namely the rotating rectangular (RR) model, the anti-tetrachiral (ATC) model, and the re-entrance or node-fibril (RON) model. The RON model is characterized by its anisotropy and can be further subdivided into the re-entrance or node-fibril stretched in the x-direction (RONx) and y-direction (RONy). The size parameters were dependent on the specific design used. A comprehensive description of the unit cell structure, design parameter categories, and fixed parameters for each model, which can impact the final structure, are provided in Figure S1, the Experimental section, and Table S1.

The uniformity of sensor dimension and response can be secured using the repeated pattern of the unit cell-based auxetic structure. However, the uniformity of sensor response is affected by the size ratio between the unit cell and light source. If the unit cell size is too small, a fabrication challenge arises due to the limited resolution of the laser

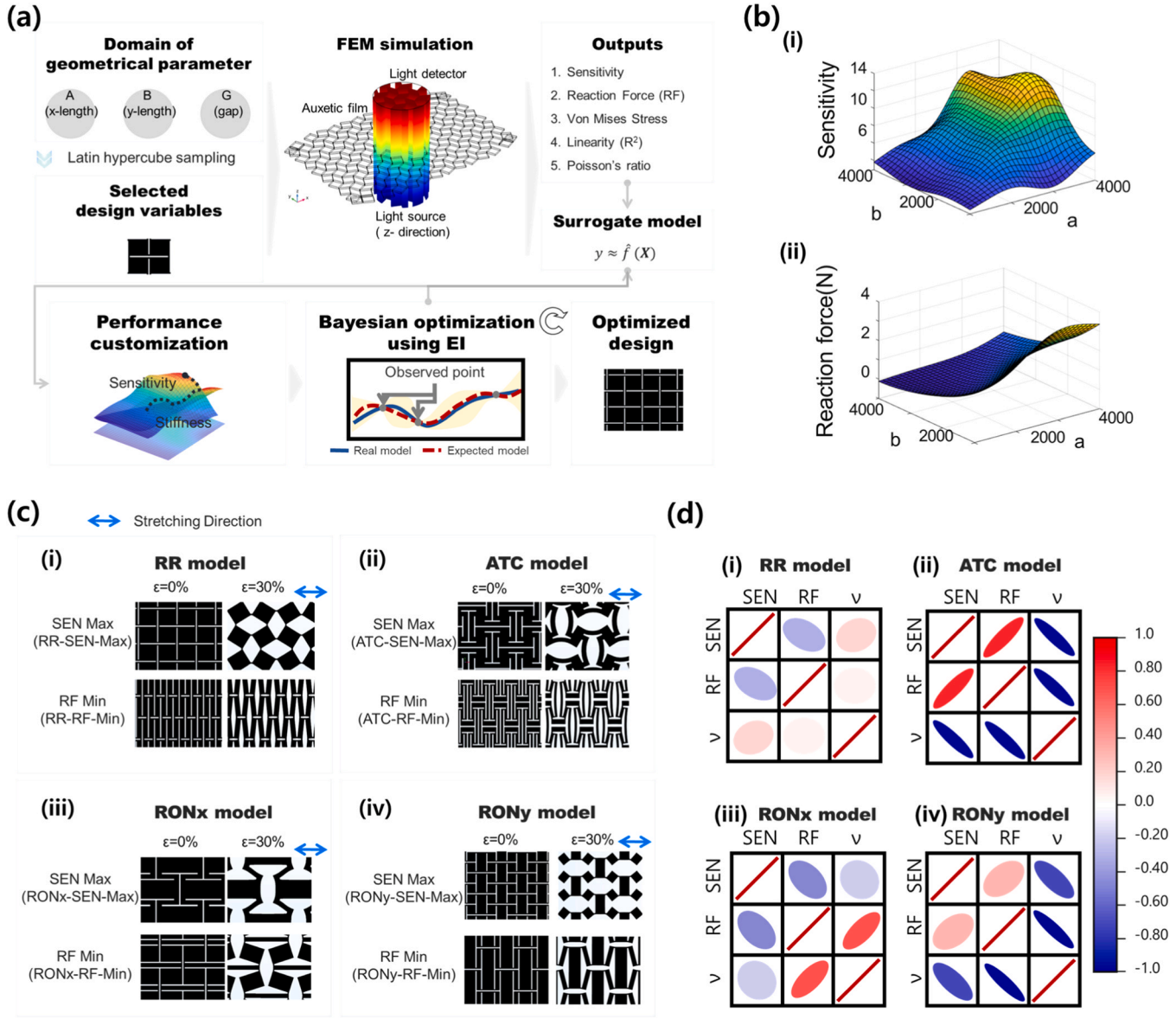



**Fig. 2.** a) Overall optimization flow using finite element method (FEM) simulation and Bayesian optimization (BO) with expectation-of-improvement function (EI) and sensor performance customization. b) Sensitivity and reaction force for rotating rectangular (RR) model c) Optimization result from the entire optimization process have been provided for each of four different designs along with their geometries for $\varepsilon = 0$ % and $\varepsilon = 30$ %. The optimal design for sensitivity maximization is referred to as SEN-Max, and that for reaction force minimization is referred to as RF-Min for each model: (i) RR model, (ii) ATC model, (iii) RONx model, (iv) RONy model. The I-shaped slits in the RONy model have been rotated by 90 degrees compared to RONx model. d) Correlation matrix for each of four different designs: (i) RR model, (ii) ATC model, (iii) RONx model, (iv) RONy model. The shape of the ellipse is calculated based on the correlation value.

cutter. On the other hand, if the unit cell is too large, being similar or larger than the light source, the uniformity of sensor response can be reduced. Therefore, a proper level of unit cell-photodetector size ratio is required, as illustrated in Figure S2 and section "Effect of the unit cell size to sensor uniformity" of the supporting information.

### 2.2. Sensor performance optimization process

Three designs were examined using FEM and BO to see how the sensor properties changed by the alteration of design parameters. From this, we were able to determine which design would maximize sensitivity and minimize reaction force for each model. The optimization flow is shown in Fig. 2**a**. Through FEM simulation, the values of sensitivity, stiffness, Von Mises stress, and linearity ($R^2$) are determined. The boundary conditions of the FEM simulation were the same as those described in reference [50].

As shown in Figure S3, light intensity (LI) in the simulation was described as the number of ray dots passing through the auxetic film ($N_{pass}$) divided by the total number of ray dots ($N_{total}$), and the response is defined by the light intensity change, depending on the external strain:

$$LI = N_{pass}/N_{total}$$

$$Response = (LI - LI_0)/LI_0$$

where $LI_0$ is the light intensity at zero strain. The response was plotted against the applied strain in the range of $\varepsilon$ = 0–30 %. The slope was defined as the sensitivity, and the coefficient of determination $R^2$ was taken as the measure of linearity. The sensitivity was calculated based on ray characterized by a hexagonal dot density. A thorough study about the effect of the dot density on the sensitivity was illustrated in Figure S4, Table S2, and section "Definition of sensitivity and conditions for ray optics simulation" of the supporting information. The reaction force was defined as the force applied to both end areas when the film was pulled and was calculated by the reaction force applied to one stretched end.

Due to the high computational cost and time required for obtaining results from FEM simulation for all possible configurations within the design space, we constructed a Gaussian process model based on FEM simulation outputs obtained from a limited sample size of 30–40 configurations within the design space. A BO model with the expectation-of-improvement function (EI) was used to find the optimized value for the model. The objective function $f(x)$ was defined as follows.

$$f(x) = -gain_1 \times sensitivity(x) + gain_2 \times reaction\ force(x)$$

where $x$ is the design vector representing the geometry parameters and $gain_1 + gain_2 = 1$. Additional constraints were applied for multi-objective optimization, namely von Mises stress of less than 2 MPa and linearity ($R^2$) greater than 0.98. The importance of the sensitivity and reaction force during optimization was expressed as gain, and different design optima can be obtained by setting each gain differently. The accuracy of the constructed surrogate model was evaluated as summarized in Table S3. More details of optimization are described in the Method section. The results show that the surrogate model accuracy has good fidelity, meaning that the optimal value from this surrogate model can be used as a sufficient substitute for a FEM model in the finite design domain.

### 2.3. Results of optimization

Fig. 2b shows the variation in the sensitivity and reaction force with changes in the geometry of the RR model. Additional design domains are also shown in Figure S5. The trends are nonlinear, depending considerably on the combination of geometric dimensions. The BO enables maintaining a balance between exploitation to reduce the cost function and exploration to reduce the uncertainty brought on by insufficient samples. Then, it can find the optimum design efficiently using the Gaussian process with much less FEM-based calculations than the conventional strategies using surrogate modeling and design optimization.

Fig. 2c shows the optimal model results when the sensitivity is maximized and when the reaction force is minimized, respectively, for each model. These results were optimized for a slit width of 100 μm. Table S4 shows the sensitivity, linearity ($R^2$), reaction force, maximum von Mises stress, and Poisson's ratio of the structure at strains of 0–30 % for each design.

Fig. 2d shows the evaluated correlation value of the optimization performance index of each design, which includes the sensitivity and reaction force as well as the Poisson's ratio - a distinguishing feature of auxetic materials. A correlation matrix of the outputs was constructed by creating samples with a homogeneous distribution over the full design space with respect to sensitivity, reaction force, and Poisson's ratio. Fig. 2d i–iv show the correlation matrices of the RR, ATC, RONx, and RONy models, respectively. The closer the shape of the ellipse in the table is to the upper-right straight line (red lines), the closer the correlation value is to 1, which indicates a positive correlation. The closer the shape of the ellipse in the table is to the upper-left straight line (blue lines), the closer the value is to −1, which indicates a negative correlation. The width and length of the ellipse are calculated based on the correlation value. The models other than the RR-model can be assumed to have higher sensitivity, as they have negative Poisson's ratios. This means that, except for the RR model, a negative Poisson's ratio could improve the sensitivity of the sensor response. For the RR model, the correlation between the sensitivity and Poisson's ratio is positive. This is because the difference in Poisson's ratio between the maximum sensitivity and the minimum reaction force cases is not large as shown in Table S4. In other words, the difference in Poisson's ratio between these two different cases is not significant, meaning that the change in Poisson's ratio is not large enough to have a substantial impact on the sensitivity of the RR model.

Figure S6 shows the effect of the slit width on the response. Since the initial light transmittance for the slit width of 30 μm is smaller than that for 100 μm by a factor of ~3.3, the response increases by a factor of ~3.3. The effect of slit width on the response is observed, but the overall trend of strain-to-light response for each design remains consistent, indicating that the design is relatively insensitive to changes in slit width and can still perform optimally. In addition, as shown in Figure S7, the results for the reaction force are not affected by the slit width, and the effect on the design optimization results is negligible.

### 2.4. Sensor fabrication process

The auxetic kirigami film was fabricated using a fiber laser and BM-PDMS. By using this technique, complex pattern structures can be produced with ease. BM-PDMS shows low transmittance, less than 1 % in the visible light region (λ=400–800 nm), despite being only 300 μm thick. PDMS cannot be cut using a fiber laser's ablation wavelength range, however it can be ablated when combined with a black pigment to create a composite form. As the absorbed energy burns the nanoparticles of the black pigment, burning occurs in the peripheral PDMS. Details of the film fabrication process, images of the cut slits, and laser ablation are shown in Figure S8 and described in the Methods section. A U-shaped cross-section of the film was produced through repeated laser ablation from the top to the bottom layer. The cross section shown in Figure S9 and the geometric size difference between the simulated model and the fabricated sensor is illustrated in Figure S10. The fabricated sensor exhibited an error of less than 5 % in the main dimensions of the geometry (the x, y-length of the unit cell).

### 2.5. Simulation result validation with fabricated sensor

The results of the design optimization achieved through simulation

and the fabricated film are compared in Fig. 3. To validate the simulation results with experimental results, the best models for sensitivity maximization and reaction force minimization were selected. According to Table S4, among the four different optimized designs, rotating rectangular model with sensitivity maximization (RR-SEN-Max) shows the best sensitivity (GF = 13.7) with good linearity ($R^2 \sim 0.99$), and re-entrance or node-fibril model stretched in the y-direction with reaction force minimization (RONy-RF-Min) has the lowest RF (0.0008 N) with good linearity ($R^2 \sim 0.99$). Fig. 3a shows a comparison of the geometric deformation under stretching for the experimental and simulation designs. The upper and lower images show the experimental and simulation results, respectively, for the RR-SEN-Max (i) and RONy-RF-Min (ii) models. The sensor response and reaction force for these two models are displayed in Fig. 3b and c, respectively. Optimal ATC model designs were also validated with experimental results, as shown in Fig. 3d and e. The experimental and simulated results for the response ($\Delta I/I_0$) are in good agreement for all the optimized designs. The experimental results for the reaction force show a consistent trend, but the values themselves vary. This variation is largely due to the boundary conditions of the gripper, which have a significant impact on the experimental results for the reaction force. As shown in Figure S11 for the other model types considered, the experimentally measured response of the sensor agrees well with the simulation results for a slit width of 30 μm. Figure S12 shows the time-series response of the RR-SEN-Max design sample to the applied strains, which confirms excellent dynamic response characteristics of the developed sensor. Also, using a test with repeated step strain inputs shown in Figure S12c and measurement data summarized in Table S5, we can calculate the response time of sensor at ε=10 % ($t_r < 73$ ms) and 30 % ($t_r < 85$ ms). Figure S13 illustrates the limit of detection (LOD) characteristics of our proposed sensor. In this experiment, we applied a stepwise strain input of 0.06 % and calculated the LOD using the equation from the literature [51], which is *Limit of detection* = $\frac{3\times S_b}{b}$ where 'b' is the slope at ε=0–0.12 % applied, '$S_b$'' is the standard deviation of the response The

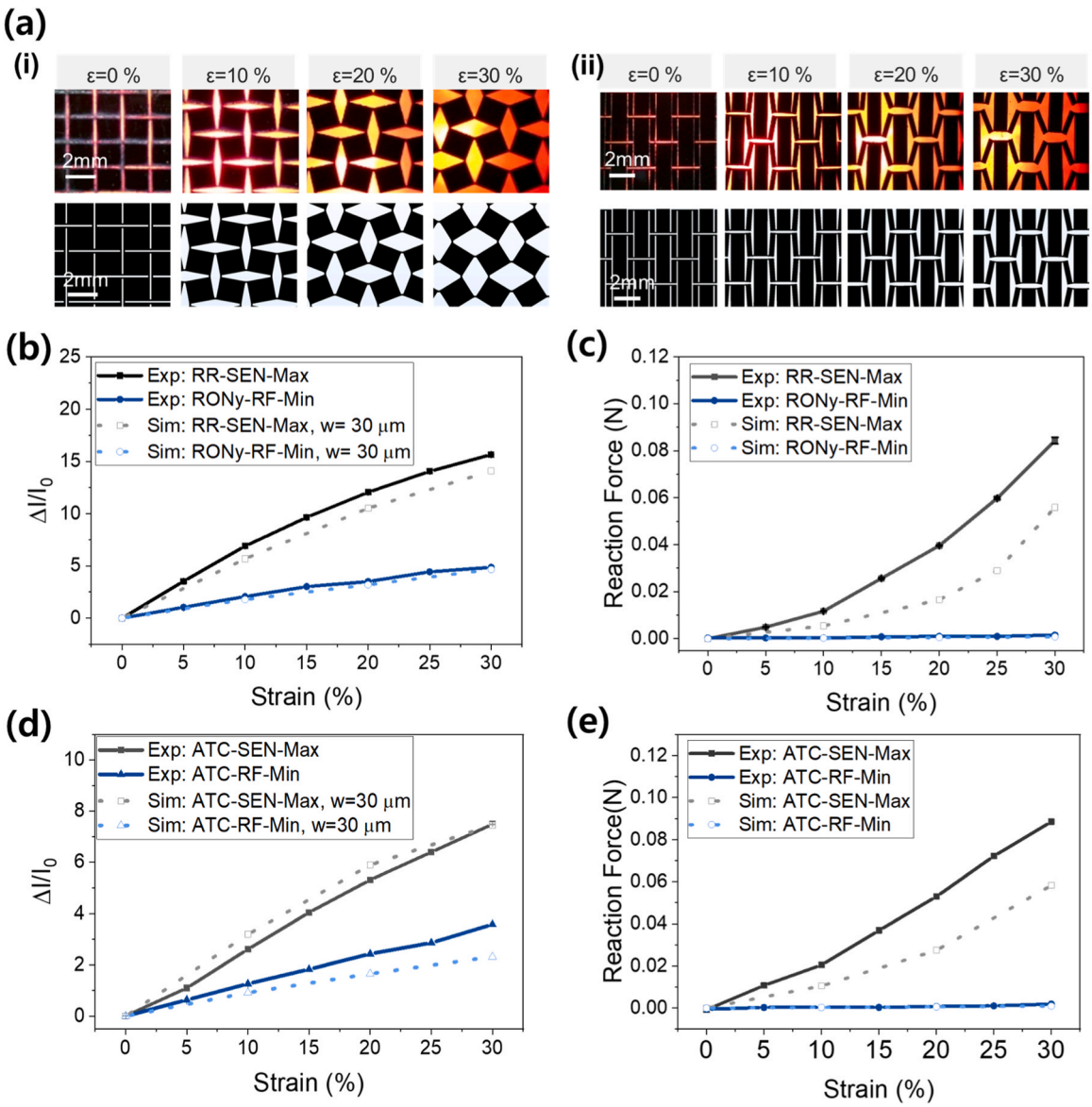



**Fig. 3.** Validation of optimization design using the laser-cut fabricated black-pigment-mixed polydimethylsiloxane (BM-PDMS) film. a) Comparison of the experimental and simulated results with the top view of the sensor film for ε = 0–30 % for (i) optimal design for rotating rectangular model with sensitivity maximization (RR-SEN-Max) model (ii) optimal design re-entrance or node-fibril stretched in the y-direction model with reaction force minimization (RONy-RF-Min) model. Comparison of the experimental and simulated results. b) Sensor responses ($\Delta I/I_0$) of RR-SEN-Max and RONy-RF-Min models. c) Sensor reaction force of RR-SEN-Max and RONy-RF-Min model. d) Sensor responses ($\Delta I/I_0$) of ATC models. e) Reaction forces of ATC models.

calculated LOD is approximately 0.045 %. Figure S14 illustrates the sensor response dependence on variations in light intensity, ranging from 11 W/m$^2$ to 70 W/m$^2$. On clear sunny days, solar intensity can reach approximately 160 W/m$^2$, while on cloudy days, it may drop to around 10 W/m$^2$. The sensor's response remains consistent, within the targeted range of light intensities. We acknowledge the need for further consideration under extreme conditions, such as very dark nights with moonlight. Under such conditions, achieving stable measurements with our sensor may require additional integration with more efficient flexible solar cells. While this aspect may pose a challenge for expanding the sensor's applicability to a wider range of real-world conditions, it is essential to note that, even with these challenges, our sensor setup exhibits stability and reliability under typical daylight conditions. Figure S15 shows the humidity dependence of the sensor response from relative humidity 25–75 %. The graph demonstrates that the sensor response variance depending on the relative humidity is negligible, with a variation of approximately 3.6 % for ε=0–30 %. Figure S16 presents the sensor's dynamic characteristics, demonstrating its durability through long-term loading-unloading tests and a 6-hour holding test to assess the sensor's drift. Specifically, Figure S16a shows the responses at 30 % strain during the first and last cycles of the 5000 loading-unloading tests, revealing an almost negligible drift of approximately 3 %. Furthermore, the results from the 6-hour holding test showed a drift of approximately 0.9 %, indicating a practically negligible level of drift. Additionally, after cyclic loading, we employed optical microscopy to observe changes of the gap where high mechanical stress. Our analysis indicated the absence of new cracks around the gaps when the structure underwent repeated loading from 0 % to 30 %, both before and after cyclic loading shown in Figure S17a-b. To thoroughly compare the mechanical properties of BM-PDMS with FEM simulation, we incorporated stress-strain curve data in Figure S17c, forming the foundation for our simulations. Based on these results, we can establish a threshold for the working range of the sensor structure as 2 MPa, which is half the fracture strength of the BM-PDMS as 4 MPa accounting for safety factor 2. The edges of the cut segment are the most vulnerable part during the stretching, and the maximum stress applied in this area varies by the geometric design. We explored the mechanical properties of two specifically optimized structures shown in Figure S18. Notably, RF-Min structure maintains stress under 2 MPa with strains over 30 %, and the maximum von Mises stress reaches 2 MPa at a strain of 170 % as shown in Figure S18a and Figure S18b. Similarly, the SEN-Max design does not experience stress levels of 2 MPa under 30 % strain and the maximum von Mises stress reaches 2 MPa at a strain of 40 % as depicted in Figure S18c and Figure S18d. This indicates that both designs are capable of functioning safely by a strain of 30 % without fracturing. In both scenarios, the highest von Mises stress, exceeding 2 MPa, is found within the edges.

### 2.6. Application of the developed sensor to SHM

To validate the broad range of potential applications of the developed sensors in accordance with their optimum self-powered sensor performances, the sensors were employed in a SHM system and HMM system. The required sensor performance differs depending on their applications. To be suitable for the rigid structure, the sensor needs to be highly sensitive even in a narrow strain range for SHM of a rigid structure because even small strains in a rigid structure can lead to cracks that impair the structural stability. In this study, we used acrylic sheets as a rigid material. We use the method aimed to validate measurement of the crack propagation in Mode I: opening mode of acrylic sheets. Considering that the fracture strain of acrylic material is minimum of 2–3 % and the limit of detection of the sensor is 0.045 %, this aligns with the low detection limit needed to adequately measure the ultimate strains of the materials. On the other hand, expandable structures may be used in a variety of deformation ranges and with relatively moderate response forces. In this case, the detection of structural deformation could be hampered if a sensor with a strong reaction force is mounted. Consequently, a sensor with a high compliance ought to be employed. To satisfy the potential applicability of the sensor into the wireless Internet of Things (IoT) system, the sensor should meet low-powered or self-powered conditions. These requirements were fulfilled by using flexible solar cell systems, which include the reference and sensing solar cells for environmental light compensation. The whole packaged system with wireless communication is depicted in Fig. 4**a**, and different designs were applied to different applications. By calibrating the intensity change of an external light source, as shown in Fig. 4b and Video S1, strain may be monitored almost irrespective of light intensity, except a low light intensity of 0.27 W/m$^2$, where the calibrated strain decreases slightly, which is noise caused by the difference in response between the sensing solar cell and the reference solar cell at low light intensity, as shown in Figure S19.

Supplementary material related to this article can be found online at doi:10.1016/j.nanoen.2024.110124.

The overall system schematic depicting fracture propagation in a rigid acrylic structure and a module for predicting inflation or deflation in expandable structures, equipped with connected sensors, is presented in Fig. 4c and more details are depicted in Figure S20. Experimental results for the SEN-Max design to monitor the fracture propagation in a rigid structure are illustrated in Fig. 4d, along with Supplementary Video S2, while the results for the RF-Min design applied to the same system are showcased in Fig. 4e. The strain values shown in Figs. 4d and 4e were calculated from the sensor's output, and these figures display the SEN-Max and RF-Min designs for the same system, respectively. Moreover, when we contrast the signal-to-noise ratio (SNR) with the logarithmic power value, we observe that the SEN-Max design exhibits an SNR of 3 dB, whereas the RF-Min design demonstrates an SNR of 1.6 dB. The RF-Min design has lower sensitivity compared to the SEN-Max design, with a difference of 1 order of magnitude, as illustrated in Figure S21. As a result, even when implemented in the same system, the noise in the BLE-Arduino module causes the signal noise in strain detection to be rather high within a limited strain range.

Supplementary material related to this article can be found online at doi:10.1016/j.nanoen.2024.110124.

Furthermore, it is crucial to acknowledge that the Arduino system introduces inherent noise into our sensor signal, impacting the data quality. For Structural Health Monitoring (SHM), high-speed data collection is generally unnecessary. Utilizing a moving average function at an increased data collection rate significantly reduced noise, enhancing signal quality and measurement accuracy, as shown in Figure S22. Fig. 4f and Video S3 demonstrate how the structure's movement is accurately measured and the BLE system alerts the user when the expansion state exceeds certain thresholds or deviates from them. The method we used to determine if the sensor had an impact on the soft and expandable structure's deformation is shown in Fig. 4g. In case of SEN-Max sensor, the expansion of the soft balloon is restrained by the sensor attached to the bottom because of high reaction force, exhibiting the ratio of the expansion change as $\delta_1$: $\delta_2$ = 1.5:1, where $\delta_1$ and $\delta_2$ represent the displacement of the balloon's expansion on the upper and lower sides of the center line, respectively. On contrary, the balloon without an attached sensor and that with a RF-Min design sensor showed an expansion ratio of $\delta_1$: $\delta_2$ = 1:1. This clearly indicates that a sensor with a strong reaction force can influence how a structure deforms. In conclusion, soft strain sensor performance can be maximized by optimizing the sensor design for specific monitoring purposes.

Supplementary material related to this article can be found online at doi:10.1016/j.nanoen.2024.110124.

### 2.7. Application of the developed sensor to HMM

In the second demonstration, the developed sensor was utilized as a self-powered HMM device for weight training and AR systems with SEN-Max design. The selected design was based on its ability to provide high

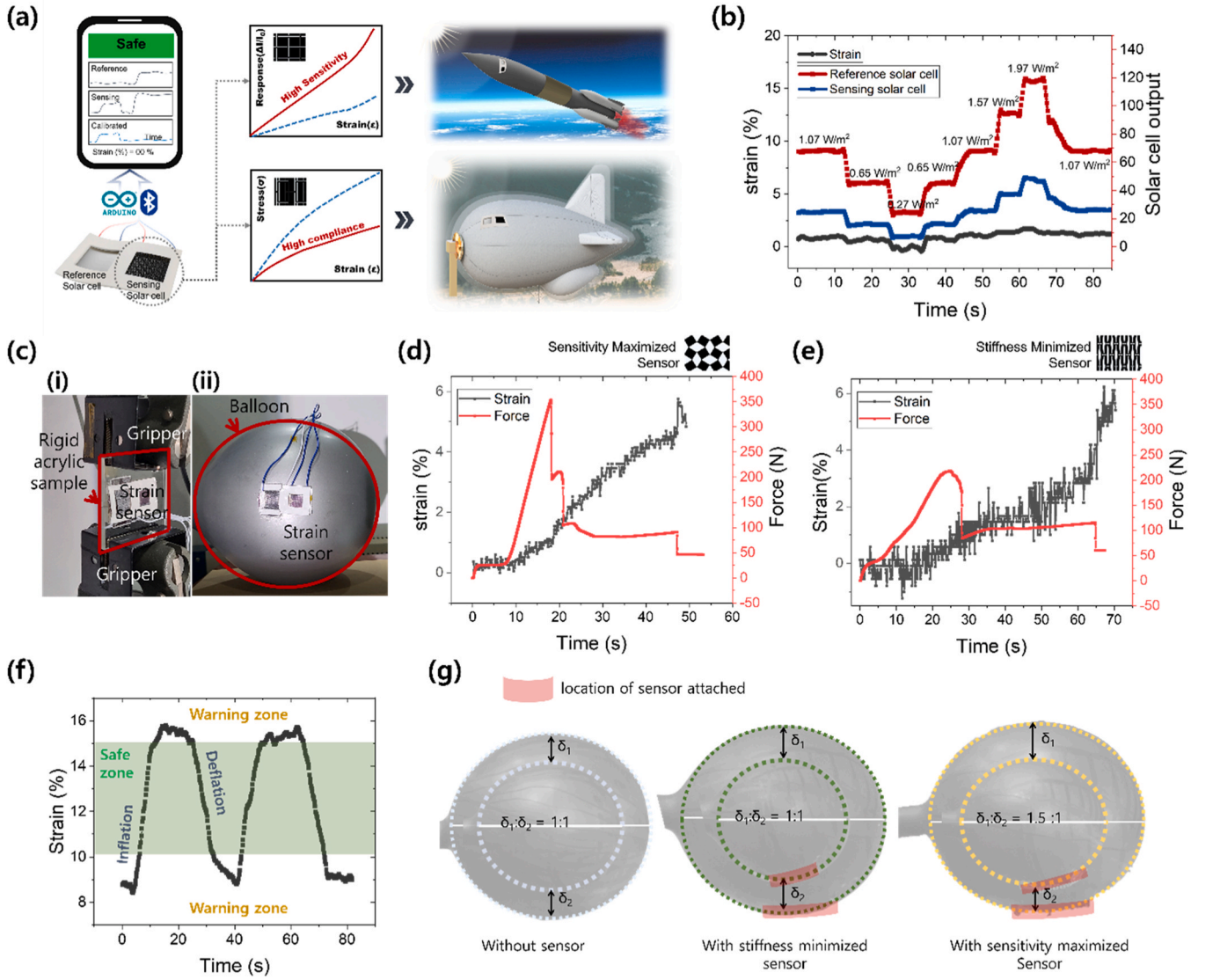



**Fig. 4.** Application of developed strain sensor to structural health monitoring (SHM). a) Overall schematic of use of SEN-Max and RF-Min designs for different purposes in self-powered wireless monitoring systems. b) Calibrated strain determined by the reference solar cell and sensing solar cell at different light source intensities. c) Overall system photograph of the experimental setup for (i) crack propagation monitoring in a rigid sample, and (ii) the alarm system during inflation and deflation of the balloon. Experimental results for crack propagation d) using the optimal design for SEN-Max design sensor, e) using the optimal design for RF-Min design. Demonstration of the alarm system during inflation and deflation of the balloon. f) Experimental results. g) Effect of sensor stiffness on the distortion of soft balloon's expansion.

sensitivity for real-time balance monitoring, essential for enhancing training efficiency and reducing accidents, while its reaction force ensures that it does not interfere with body motion during exercise. In the context of measuring human body motion, it is essential to consider the range of strain required. Literatures [52–55] have suggested that the knee joint, which exhibits significant motions, experiences an approximate maximum average longitudinal strain of around 20 % on the skin. The auxetic kirigami sensor itself provides enough compliance to avoid body motion interference. Additionally, proper joint bending positions are essential to avoid joint injuries during exercise, making the sensor's monitoring capabilities even more important.

In the future, sports and entertainment systems are expected to incorporate AR/VR technologies, and the inclusion of joint bending monitoring systems could potentially enable the integration of motion monitoring with these systems. This presents a promising application for sensor technology in the field of sports and entertainment. Herein, we first made a system that can monitor postural balance in real-time, communicate via Bluetooth, and analyze/display data using a mobile application software as shown in Fig. 5**a-i**. Based on the collected data, a real-time warning about the degree of postural imbalance can be generated. In specific, balance monitoring was applied to a seated chest press exercise. The sensors were attached to the pectoralis major (i.e. pecs), which are the primary target muscles of this exercise, as illustrated in Fig. 5b. Before starting the exercise, the pecs are in a stretched state; hence, the sensors are under tensile strain with gap opening. When the machine is placed in the correct position and balance, both pecs contract similarly. However, if the machine is pushed in an imbalanced position, the contraction of the pecs may differ between the left and right sides, as depicted in Fig. 5b-ii. As seen in Fig. 5c and Video S4, the sensors attached to the chest were designed to be very sensitive to detect changes in muscular contraction. The muscular strains recorded by both sensors throughout the workout were used to calculate the Pearson correlation coefficient (PCC), which was used to determine the degree of balance. The closer PCC value is to 1, the more positively correlated the muscle strains are, and the closer the PCC is to −1, the more negatively correlated they are. Fig. 5c illustrates that the PCC value is

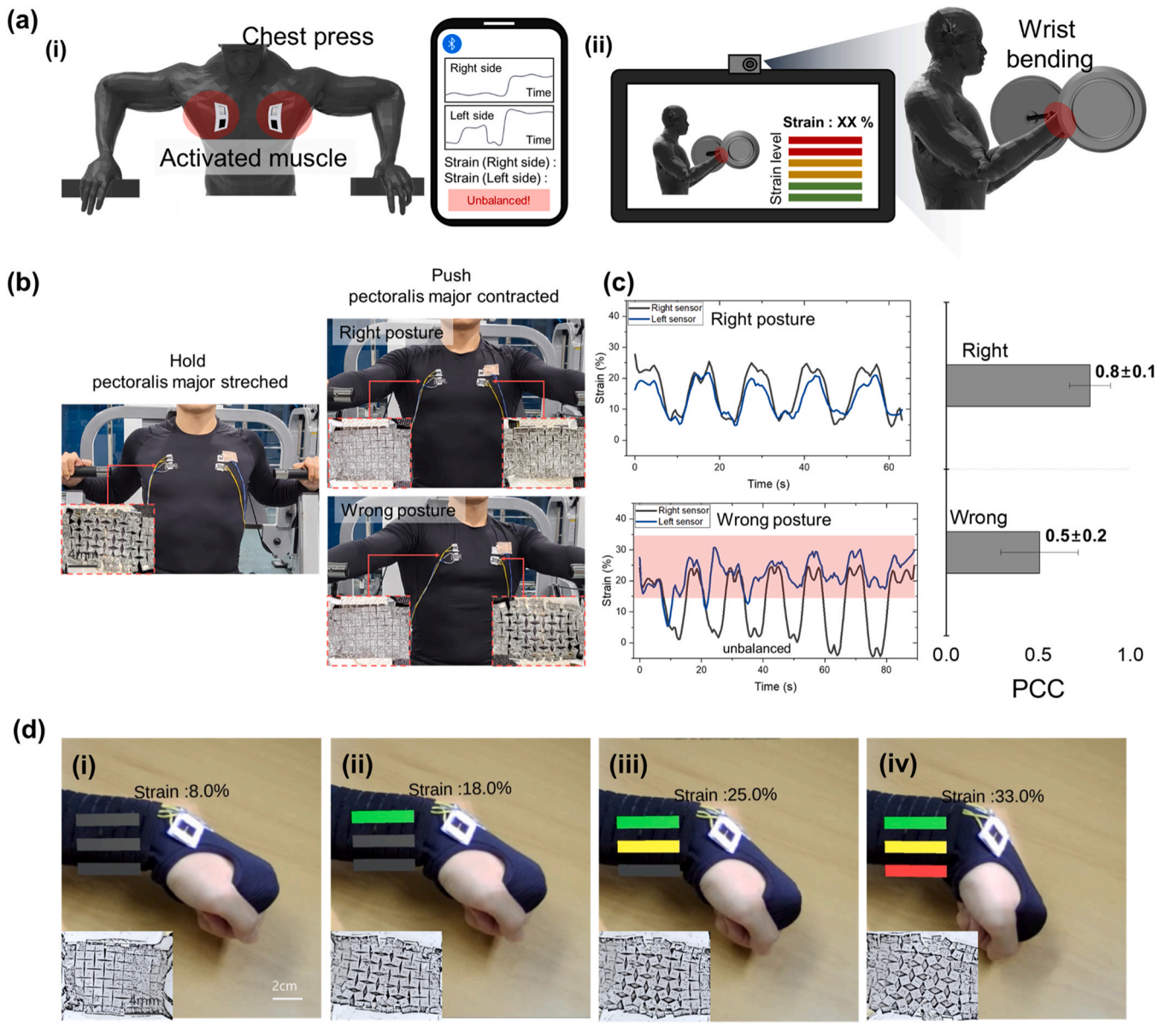



**Fig. 5.** Application of the developed strain sensor to human motion monitoring (HMM) and augmented reality (AR) systems. a) Schematic of the sensor system on HMM. (i) Workout balance monitoring system using Bluetooth communication. (ii) Wrist bending monitoring AR system. b) Photograph for seated chest press training with right and wrong postures. c) Experimental results of right and wrong postures and the Pearson correlation coefficient (PCC) value of each posture. d) Photograph capture of AR video system during the wrist bending detection and displaying the sensor value on the AR display. (i) Small bending with a strain of 8 %, (ii) Small medium bending with a strain of 18 %, (iii) Medium bending with a strain of 25 %, (iv) Large bending with a strain of 33 %.

approximately 0.8 when using proper posture, which indicates a strong positive correlation between muscle strains. In contrast, when using an incorrect posture, the PCC value is lower at approximately 0.5, suggesting a weaker positive correlation between muscle strains. This experiment shows that a sensor with a high sensitivity may be utilized in HMM applications to assess the postural balance during exercise.

Supplementary material related to this article can be found online at doi:10.1016/j.nanoen.2024.110124.

The sensor was also used on human subjects, and the resulting strain values were displayed on an AR monitor located near the wrist, as shown in Fig. 5a-ii. Specifically, the sensor attached to the wrist measured its strain, which was then reflected on the AR monitor. As shown in Fig. 5d, the display on the monitor included a gray bar that lit up for strains between 0 % and 10 %, green for strains between 10 % and 20 %, yellow for strains between 20 % and 30 %, and red for strains greater than 30 %. This visual display remained steady even when the camera moved, as illustrated in Video S5. These results demonstrate the potential of integrating the sensor into an AR/VR system to provide a vivid feedback mechanism for exercise. Furthermore, the sensor's capability extends beyond detecting wide-range motions to identifying subtle variations (~5 %) in skin stretch. This proficiency is exemplified in the detection of minimal finger movements through the stretch of skin on the back of the hand and the monitoring of breathing patterns through ribcage motion detection. These functionalities highlight the sensor's adaptability to a broad spectrum of human motion detection. The successful identification of these nuanced skin stretches is presented in Figure S23, Video S6, and Video S7, affirming the sensor's exceptional sensitivity and its broad applicative potential in capturing a diverse array of human motions.

Supplementary material related to this article can be found online at doi:10.1016/j.nanoen.2024.110124.

## 3. Discussion and conclusion

In this research, we developed an optimal design for a piezo-transmittance strain sensor by multi-objective optimization approach which considered both the sensor's sensitivity and compliance for various applications and then evaluated the performance of the optimized design in SHM, HMM, and AR. Comparing with other typical type soft strain sensors, piezo-transmittance strain sensors [19] have been introduced based on their high sensitivity, linearity, low hysteresis, and stability. These sensors initially gained recognition for their performance characteristics but have subsequently demonstrated significant potential as self-powered strain sensors through integration with solar cells. This potential has positioned them as promising candidates for low-power and self-powered systems. Traditional resistive strain sensors have been extensively researched and offer high sensitivity and versatility owing to their simple system setup and use of various materials. However, it is important to note that the reported high sensitivity often varies with sensing range, and long-term stability can be compromised, particularly with specific materials. Additionally, the fabrication of such sensors can introduce additional energy consumption in the circuitry, posing limitations in constructing low-power or self-powered systems. Capacitive strain sensors have also been extensively utilized. They exhibit advantages such as minimal susceptibility to external noise, linear response characteristics, and stability. However, due to their mechanism, these sensors are more commonly applied as pressure sensors, as they have a maximum gauge factor of 1 for strain measurement, limiting their use as strain sensors. The optical fiber strain sensors can be applied in various contexts, but they require an additional photo-coupler system that necessitates a power source and also demands a complex peak analysis system. The comparison table with the other sensor mechanisms is illustrated in Table S6. Based on these advantages, this study is the first attempt to optimize the design of a piezo-transmittance type strain sensor using an auxetic kirigami structure. We optimized our proposed design, which guarantees sensor uniformity and fidelity through a pre-designed gap opening mechanism, by selecting rotating rectangular, chiral, and re-entrance structures from various auxetic structures.

We developed a surrogate model for a piezo-transmittance strain sensor using FEM simulation outputs of a limited sample size to optimize the objective function, which considers the sensor response and compliance with additional constraints. The accuracy of the constructed surrogate model was evaluated and found to have good fidelity, allowing for obtaining different design optimum by setting each gain differently. Multi-objective BO was used to maximize either sensitivity or compliance, taking advantage of its high sampling efficiency, which allows it to concentrate on sampling within the candidate group rather than random design space. By identifying the design features that enhance sensor sensitivity and minimize the reaction force, we fabricated the optimized design using laser-cut BM-PDMS and validated the FEM simulated performance results by experiment. In SHM applications, where the range of measured strain is typically small, it is more critical for a sensor to have high sensitivity over a small strain range than for the sensor's reaction force to be low. Our research showed that designing a sensor with maximum sensitivity can improve the signal-to-noise ratio (SNR) within the measurement system. On the other hand, when monitoring a structure with a high expansion rate, it is crucial to minimize the restriction of the structure's movement by attached sensors. Our study confirmed that a sensor with minimum reaction force attached to an inflatable structure with a high expansion rate can minimize structural distortion. In HMM applications, the wearable sensor could measure imbalance during exercise in sports monitoring systems and could be integrated into AR systems to display the joint motion. It is expected that our sensor design can be optimized for different purposes and is suitable for diverse applications, such as wireless wearable systems, low-power sensing systems, space-sector applications, healthcare monitoring systems, and industrial Internet-of-Things (IoT) systems.

## 4. Materials and methods

*Film fabrication and characterization*: To create a light blocking polydimethylsiloxane (PDMS) film, the PDMS material was mixed with a black pigment (Silc pig, Smooth-on, Inc., USA) at a concentration of 10 % by weight using a planetary mixer (ARE-310, Thinky, Inc., USA) for a period of 5 minutes. The mixture was then cooled for 15 minutes and the process was repeated four times. Then a film was spin-coated (250 rpm, 60 s) on the donor substrate and transferred to the glass substrate for laser cutting. The auxetic pattern was engraved by fiber laser (REXBOT-M20D, NTRexLAB, Korea) with a wavelength of 1064 nm at various scanning powers and speeds. The cross section was observed using a 3D laser scanning confocal microscope (VX-X1050, KEYENCE, Japan). The sizes of the top and bottom sides were ~100 μm and ~30 μm, respectively. The sensor response was compared with the simulation results for a 30 μm slit based on the constructed geometry, where the assumption was that light passes through the thinnest side of the geometric structure at the initial state.

*Optimization*: Bayesian optimization (BO) was used to optimize the sensor design. It uses the expectation-of-improvement (EI) as acquisition function to determine the optimal design. BO is advantageous because it reduces the computational cost of the response evaluation compared to traditional methods, such as FEM simulation. To generate the surrogate model, FEM simulation was used to calculate the sample data evaluation process with 30–40 samples for each design obtained by Latin hypercube sampling in the design space. The design space was determined for three different design models: rotating rectangular (RR), anti-tetrachiral (ACT), and re-entrance or node-fibril (RON), as shown in Table S1. The geometry was created in various combinations within the boundary condition of the design variable. Five outputs were extracted in the studied data: sensitivity, reaction force, von Mises stress, linearity of transmission change, and Poisson's ratio. Based on the calculated outputs, a Gaussian process model was built. The optimal value for the model with the genetic algorithm was discovered using a BO model with the EI function. The objective is to maximize the sensitivity and/or to minimize the reaction force required to pull the film, given the conditions of high linearity ($R^2 > 0.98$) and a limit on the von Mises stress (< 2 MPa). The objective function can be written as follows:

$$f(\boldsymbol{x}) = -gain_1 \times sensitivity(\boldsymbol{x}) + gain_2 \times reaction\ force(\boldsymbol{x})$$

where $\boldsymbol{x}$ is the design vector representing the geometry parameters and $gain_1 + gain_2 = 1$.

*Sensor characterization*: A universal testing machine (AGS-X plus series, Shimadzu, Japan) was used to conduct stress-strain tests and response force tests on auxetic patterned film. The samples were prepared in dog bone shapes following the guidelines outlined in the ASTM D412 standard for stress-strain testing of materials. In order to evaluate the performance of the sensor, the film was attached to both ends of a uniaxial linear stage. A visible-range ($\lambda$ = 400–800 nm) solar illuminator (LAX-C100 Xenon light source, Asahi Spectra Co., Ltd., Inc., Japan) was positioned at 100 mm above the film. A power detector (S120C, Thorlabs, Inc., USA) was positioned directly beneath the film to monitor changes in the amount of light transmission.

*Self-powered wireless sensor for SHM and HMM*: An Arduino board, a smartphone application created using MIT App Inventor (App Inventor 2, Google, USA), and a commercial solar cell (ONP1.2–12×24, PowerFilm, Inc., USA) were used to construct a self-powered wireless sensor. The solar cell's current output was converted into a voltage signal through a trans-impedance amplifier circuit. The voltage signal was then transmitted to a mobile device using Bluetooth low-energy (BLE 4.0) communication. Custom acrylic replicas were fabricated to emulate the intricate architecture of an artificial satellite system. To explore the viability of these replicas for use in satellite systems, a tensile tester

(AGS-X plus series, Shimadzu, Japan) was employed to apply measured amounts of tensile stress to the acrylic specimens. Additionally, commercial balloons were employed to simulate an aerostat system, with an air gun utilized to inflate the balloons, thus demonstrating the potential use for aerostat systems. The sensory data gathered was collected by a smartphone when every demonstration was conducted. For the HMM experiment, a similar setup with a commercial rash guard and wrist guards was employed to monitor postural balance. The experiment was approved by institutional review board of KAIST (IRB No. KH2021–004).

*AR system for HMM*: The solar cell utilized in the study was identical to the one used in the self-powered wireless system. Unity software (Unity Software Inc., USA) was employed to develop the AR (augmented reality) system, and the Vuforia Enterprise AR software (PTC Inc., USA) was utilized to incorporate an Arduino board for data sensing into the Unity server.

## CRediT authorship contribution statement

**Jimin Gu:** Writing – review & editing, Writing – original draft, Visualization, Methodology, Conceptualization. **Yongsu Jung:** Writing – original draft, Visualization, Formal analysis. **Junseong Ahn:** Writing – review & editing, Validation, Conceptualization. **Jihyeon Ahn:** Visualization, Methodology. **Jungrak Choi:** Writing – review & editing, Methodology. **Byeongmin Kang:** Validation, Methodology. **Yongrok Jeong:** Writing – review & editing, Visualization, Conceptualization. **Ji-Hwan Ha:** Writing – review & editing, Conceptualization. **Taehwan Kim:** Methodology. **Young Jung:** Conceptualization. **Jaeho Park:** Validation, Conceptualization. **Jiyoung Jung:** Software. **Seunghwa Ryu:** Software. **Ikjin Lee:** Validation, Formal analysis. **Inkyu Park:** Writing – review & editing, Supervision, Resources, Investigation, Funding acquisition.

## Declaration of Competing Interest

The authors declare that they have no known competing financial interests or personal relationships that could have appeared to influence the work reported in this paper.

## Data availability

Data will be made available on request.

## Acknowledgements

This work was supported by the National Research Foundation of Korea (NRF) grant funded by the Korea government(MSIT) (No. 2021R1A2C3008742), Ministry of Culture, Sports and Tourism and Korea Creative Content Agency (Project Number: R2021040018), and the Technology Innovation Program (00144157, Development of Heterogeneous Multi-Sensor Micro-System Platform) funded By the Ministry of Trade, Industry & Energy (MOTIE, korea).

## Appendix A. Supporting information

Supplementary data associated with this article can be found in the online version at doi:10.1016/j.nanoen.2024.110124.

## References

[1] M.S. Kim, Y. Lee, J. Ahn, S. Kim, K. Kang, H. Lim, B.S. Bae, I. Park, Skin-like omnidirectional stretchable platform with negative poisson's ratio for wearable strain–pressure simultaneous sensor, Adv. Funct. Mater. 33 (2023) 1–10, https://doi.org/10.1002/adfm.202208792.

[2] Y. Jung, J. Choi, W. Lee, J.S. Ko, I. Park, H. Cho, Irregular microdome structure-based sensitive pressure sensor using internal popping of microspheres, Adv. Funct. Mater. 32 (2022) 1–12, https://doi.org/10.1002/adfm.202201147.

[3] A. Abramson, C.T. Chan, Y. Khan, A. Mermin-Bunnell, N. Matsuhisa, R. Fong, R. Shad, W. Hiesinger, P. Mallick, S.S. Gambhir, Z. Bao, A flexible electronic strain sensor for the real-time monitoring of tumor regression, Sci. Adv. 8 (2022) 6550, https://doi.org/10.1126/sciadv.abn6550.

[4] S.A. Dual, B. Llerena Zambrano, S. Sündermann, N. Cesarovic, M. Kron, K. Magkoutas, J. Hengsteler, V. Falk, C. Starck, M. Meboldt, J. Vörös, M. Schmid Daners, Continuous heart volume monitoring by fully implantable soft strain sensor, Adv. Health Mater. 9 (2020) 2000855, https://doi.org/10.1002/adhm.202000855.

[5] S. Lin, S. Hu, W. Song, M. Gu, J. Liu, J. Song, Z. Liu, Z. Li, K. Huang, Y. Wu, M. Lei, H. Wu, An ultralight, flexible, and biocompatible all-fiber motion sensor for artificial intelligence wearable electronics, Npj Flex. Electron. 6 (2022), https://doi.org/10.1038/s41528-022-00158-8.

[6] Y. Jeong, J. Gu, J. Byun, J. Ahn, J. Byun, K. Kim, J. Park, J. Ko, J. Jeong, M. Amjadi, I. Park, Ultra-wide range pressure sensor based on a microstructured conductive nanocomposite for wearable workout monitoring, Adv. Health Mater. 10 (2021) 2001461, https://doi.org/10.1002/adhm.202001461.

[7] M. Amjadi, K.-U. Kyung, I. Park, M. Sitti, Stretchable, skin-mountable, and wearable strain sensors and their potential applications: a review, Adv. Funct. Mater. 26 (2016) 1678–1698, https://doi.org/10.1002/adfm.201504755.

[8] V. Sanchez, C.J. Walsh, R.J. Wood, TextiLe Technology for Soft Robotic and Autonomous Garments, Adv. Funct. Mater. 31 (2021) 2008278, https://doi.org/10.1002/adfm.202008278.

[9] H. Kim, Y.T. Kwon, H.R. Lim, J.H. Kim, Y.S. Kim, W.H. Yeo, Recent advances in wearable sensors and integrated functional devices for virtual and augmented reality applications, Adv. Funct. Mater. 31 (2021) 1–12, https://doi.org/10.1002/adfm.202005692.

[10] Z. Zhang, T. He, M. Zhu, Z. Sun, Q. Shi, J. Zhu, B. Dong, M.R. Yuce, C. Lee, Deep learning-enabled triboelectric smart socks for IoT-based gait analysis and VR applications, Npj Flex. Electron. 4 (2020) 29, https://doi.org/10.1038/s41528-020-00092-7.

[11] L. Wu, J. Ahn, J. Choi, J. Gu, X. Li, O. Gul, Z.J. Zhao, L. Qian, B. Yu, I. Park, Customizable self-powered pressure sensor based on piezo-transmittance of tilted structures, Nano Energy 109 (2023) 108299, https://doi.org/10.1016/j.nanoen.2023.108299.

[12] J. Gu, J. Ahn, J. Jung, S. Cho, J. Choi, Y. Jeong, J. Park, S. Hwang, I. Cho, J. Ko, J.-H. Ha, Z.-J. Zhao, S. Jeon, S. Ryu, J.-H. Jeong, I. Park, Self-powered strain sensor based on the piezo-transmittance of a mechanical metamaterial, Nano Energy 89 (2021) 106447, https://doi.org/10.1016/j.nanoen.2021.106447.

[13] B. Mahanty, S.K. Ghosh, S. Jana, Z. Mallick, S. Sarkar, D. Mandal, ZnO nanoparticle confined stress amplified all-fiber piezoelectric nanogenerator for self-powered healthcare monitoring, Sustain Energy Fuels 5 (2021) 4389–4400, https://doi.org/10.1039/d1se00444a.

[14] M. Chen, Z. Wang, Q. Zhang, Z. Wang, W. Liu, M. Chen, L. Wei, Self-powered multifunctional sensing based on super-elastic fibers by soluble-core thermal drawing, Nat. Commun. 12 (2021) 1416, https://doi.org/10.1038/s41467-021-21729-9.

[15] S. Farhangdoust, G. Georgeson, J.B. Ihn, F.K. Chang, Kirigami auxetic structure for high efficiency power harvesting in self-powered and wireless structural health monitoring systems, Smart Mater. Struct. 30 (2020), https://doi.org/10.1088/1361-665X/abcaaf.

[16] J. Choi, D. Kwon, B. Kim, K. Kang, J. Gu, J. Jo, K. Na, J. Ahn, D. Del Orbe, K. Kim, J. Park, J. Shim, J.Y. Lee, I. Park, Wearable self-powered pressure sensor by integration of piezo-transmittance microporous elastomer with organic solar cell, Nano Energy 74 (2020) 104749, https://doi.org/10.1016/j.nanoen.2020.104749.

[17] Y. Hu, C. Xu, Y. Zhang, L. Lin, R.L. Snyder, Z.L. Wang, A nanogenerator for energy harvesting from a rotating tire and its application as a self-powered pressure/speed sensor, Adv. Mater. 23 (2011) 4068–4071, https://doi.org/10.1002/adma.201102067.

[18] Z. Yan, L. Wang, Y. Xia, R. Qiu, W. Liu, M. Wu, Y. Zhu, S. Zhu, C. Jia, M. Zhu, R. Cao, Z. Li, X. Wang, Flexible high-resolution triboelectric sensor array based on patterned laser-induced graphene for self-powered real-time tactile sensing, Adv. Funct. Mater. 31 (2021) 1–9, https://doi.org/10.1002/adfm.202100709.

[19] J. Gu, D. Kwon, J. Ahn, I. Park, Wearable strain sensors using light transmittance change of carbon nanotube-embedded elastomers with microcracks, ACS Appl. Mater. Interfaces 12 (2020) 10908–10917, https://doi.org/10.1021/acsami.9b18069.

[20] Q. Zhai, Y. Yang, Highly stretchable variable-transmittance skin for ultrasensitive and wearable strain sensing, 1700161, Adv. Mater. Technol. (2017) 1700161, https://doi.org/10.1002/admt.201700161.

[21] T. Huang, Y. Long, Z. Dong, Q. Hua, J. Niu, X. Dai, J. Wang, J. Xiao, J. Zhai, W. Hu, UltralighT, Elastic, Hybrid Aerogel for Flexible/wearable Piezoresistive Sensor and Solid–solid/gas–solid Coupled Triboelectric Nanogenerator, Adv. Sci. (2022), https://doi.org/10.1002/advs.202204519.

[22] J. Ma, P. Wang, H. Chen, S. Bao, W. Chen, H. Lu, Highly sensitive and large-range strain sensor with a self-compensated two-order structure for human motion detection, ACS Appl. Mater. Interfaces 11 (2019) 8527–8536, https://doi.org/10.1021/acsami.8b20902.

[23] Y. Zhou, P. Zhan, M. Ren, G. Zheng, K. Dai, L. Mi, C. Liu, C. Shen, Significant stretchability enhancement of a crack-based strain sensor combined with high sensitivity and superior durability for motion monitoring, ACS Appl. Mater. Interfaces 11 (2019) 7405–7414, https://doi.org/10.1021/acsami.8b20768.

[24] S. Zhang, L. Wen, H. Wang, K. Zhu, M. Zhang, Vertical CNT-Ecoflex nanofins for highly linear broad-range-detection wearable strain sensors, J. Mater. Chem. C. Mater. 6 (2018) 5132–5139, https://doi.org/10.1039/c7tc05571d.

[25] S. Li, R. Li, O.G. González, T. Chen, X. Xiao, Highly sensitive and flexible piezoresistive sensor based on c-MWCNTs decorated TPU electrospun fibrous network for human motion detection, Compos Sci. Technol. 203 (2021), https://doi.org/10.1016/j.compscitech.2020.108617.
[26] Y. Kim, K.P. Faseela, S.Y. Yang, K. Kim, H.J. Yu, J.Y. Lim, J.G. Do, H.R. Choi, J. H. Hwang, S. Baik, Excellent reversibility of resistive nanocomposite strain sensor composed of silver nanoflowers, polyurethane, and polyester rubber band, Compos Sci. Technol. 221 (2022), https://doi.org/10.1016/j.compscitech.2022.109305.
[27] Y. Zheng, Z. Yu, G. Mao, Y. Li, D. Pravarthana, W. Asghar, Y. Liu, S. Qu, J. Shang, R. Li, A wearable capacitive sensor based on ring/disk-shaped electrode and porous dielectric for noncontact healthcare monitoring, Glob. Chall. 4 (2020), https://doi.org/10.1002/gch2.201900079.
[28] J. Qin, L.J. Yin, Y.N. Hao, S.L. Zhong, D.L. Zhang, K. Bi, Y.X. Zhang, Y. Zhao, Z. M. Dang, Flexible and stretchable capacitive sensors with different microstructures, Adv. Mater. 33 (2021), https://doi.org/10.1002/adma.202008267.
[29] X. Wang, Y. Deng, P. Jiang, X. Chen, H. Yu, Low-hysteresis, pressure-insensitive, and transparent capacitive strain sensor for human activity monitoring, Micro Nanoeng. 8 (2022), https://doi.org/10.1038/s41378-022-00450-7.
[30] H. Xu, Y. Lv, D. Qiu, Y. Zhou, H. Zeng, Y. Chu, An ultra-stretchable, highly sensitive and biocompatible capacitive strain sensor from an ionic nanocomposite for on-skin monitoring, Nanoscale 11 (2019) 1570–1578, https://doi.org/10.1039/c8nr08589g.
[31] R. Nur, N. Matsuhisa, Z. Jiang, M.O.G. Nayeem, T. Yokota, T. Someya, A highly sensitive capacitive-type strain sensor using wrinkled ultrathin gold films, Nano Lett. 18 (2018) 5610–5617, https://doi.org/10.1021/acs.nanolett.8b02088.
[32] L. Cai, L. Song, P. Luan, Q. Zhang, N. Zhang, Q. Gao, D. Zhao, X. Zhang, M. Tu, F. Yang, W. Zhou, Q. Fan, J. Luo, W. Zhou, P.M. Ajayan, S. Xie, Super-stretchable, transparent carbon nanotube-based capacitive strain sensors for human motion detection, Sci. Rep. 3 (2013) 3048, https://doi.org/10.1038/srep03048.
[33] L. Bahin, M. Tourlonias, M.A. Bueno, K. Sharma, R.M. Rossi, Smart textiles with polymer optical fibre implementation for in-situ measurements of compression and bending, Sens Actuators A Phys. 350 (2023), https://doi.org/10.1016/j.sna.2022.114117.
[34] A. Leber, C. Dong, S. Laperrousaz, H. Banerjee, M.E.M.K. Abdelaziz, N. Bartolomei, B. Schyrr, B. Temelkuran, F. Sorin, Highly integrated multi-material fibers for soft robotics, Adv. Sci. (2022), https://doi.org/10.1002/advs.202204016.
[35] K. Jakubowski, W. Kerkemeyer, E. Perret, M. Heuberger, R. Hufenus, Liquid-core polymer optical fibers for luminescent waveguide applications, Mater. Des. 196 (2020), https://doi.org/10.1016/j.matdes.2020.109131.
[36] S. Lantean, M. Lo Preti, L. Beccai, Stretchable reflective coating for soft optical waveguides and sensors, Soft Matter 18 (2022) 7827–7837, https://doi.org/10.1039/d2sm00869f.
[37] J. Guo, C. Yang, Q. Dai, L. Kong, Soft and stretchable polymeric optical waveguide-based sensors for wearable and biomedical applications, Sens. (Switz. ) 19 (2019), https://doi.org/10.3390/s19173771.
[38] H. Yang, J. Li, K.Z. Lim, C. Pan, T. Van Truong, Q. Wang, K. Li, S. Li, X. Xiao, M. Ding, T. Chen, X. Liu, Q. Xie, P.V. y Alvarado, X. Wang, P.-Y. Chen, Automatic strain sensor design via active learning and data augmentation for soft machines, Nat. Mach. Intell. 4 (2022) 84–94, https://doi.org/10.1038/s42256-021-00434-8.
[39] J. Gu, J. Ahn, J. Jung, S. Cho, J. Choi, Y. Jeong, J. Park, S. Hwang, I. Cho, J. Ko, J. H. Ha, Z.J. Zhao, S. Jeon, S. Ryu, J.H. Jeong, I. Park, Self-powered strain sensor based on the piezo-transmittance of a mechanical metamaterial, Nano Energy 89 (2021) 106447, https://doi.org/10.1016/j.nanoen.2021.106447.
[40] A. Slann, W. White, F. Scarpa, K. Boba, I. Farrow, Cellular plates with auxetic rectangular perforations, Phys. Status Solidi B Basic Res 252 (2015) 1533–1539, https://doi.org/10.1002/pssb.201451740.
[41] L. Mizzi, K.M. Azzopardi, D. Attard, J.N. Grima, R. Gatt, Auxetic metamaterials exhibiting giant negative Poisson's ratios, Phys. Status Solidi (RRL) - Rapid Res. Lett. 9 (2015) 425–430, https://doi.org/10.1002/pssr.201510178.
[42] J.N. Grima, L. Mizzi, K.M. Azzopardi, R. Gatt, Auxetic perforated mechanical metamaterials with randomly oriented cuts, Adv. Mater. 28 (2016) 385–389, https://doi.org/10.1002/adma.201503653.
[43] J.N. Grima, R. Gatt, Perforated sheets exhibiting negative Poisson's ratios, Adv. Eng. Mater. 12 (2010) 460–464, https://doi.org/10.1002/adem.201000005.
[44] J.N. Grima, K.E. Evans, Auxetic behavior from rotating squares, J. Mater. Sci. Lett. 19 (2000) 1563–1565, https://doi.org/10.1023/A:1006781224002.
[45] R. Gatt, D. Attard, P.S. Farrugia, K.M. Azzopardi, L. Mizzi, J.P. Brincat, J.N. Grima, A realistic generic model for anti-tetrachiral systems, Phys. Status Solidi B Basic Res 250 (2013) 2012–2019, https://doi.org/10.1002/pssb.201384246.
[46] M. Mir, M.N. Ali, J. Sami, U. Ansari, Review of mechanics and applications of auxetic structures, Adv. Mater. Sci. Eng. 2014 (2014) 1–17, https://doi.org/10.1155/2014/753496.
[47] S. Shan, S.H. Kang, Z. Zhao, L. Fang, K. Bertoldi, Design of planar isotropic negative Poisson's ratio structures, Extrem. Mech. Lett. 4 (2015) 96–102, https://doi.org/10.1016/j.eml.2015.05.002.
[48] X. Ren, R. Das, P. Tran, T.D. Ngo, Y.M. Xie, Auxetic metamaterials and structures: a review, Smart Mater. Struct. 27 (2018) 023001, https://doi.org/10.1088/1361-665X/aaa61c.
[49] S. Daulton, D. Eriksson, M. Balandat, E. Bakshy, Multi-Objective Bayesian Optimization over High-Dimensional Search Spaces, (2021).
[50] J. Gu, J. Ahn, J. Jung, S. Cho, J. Choi, Y. Jeong, J. Park, S. Hwang, I. Cho, J. Ko, J.-H. Ha, Z.-J. Zhao, S. Jeon, S. Ryu, J.-H. Jeong, I. Park, Self-powered strain sensor based on the piezo-transmittance of a mechanical metamaterial, Nano Energy 89 (2021) 106447, https://doi.org/10.1016/j.nanoen.2021.106447.
[51] A. Shrivastava, V. Gupta, Methods for the determination of limit of detection and limit of quantitation of the analytical methods, Chron. Young Sci. 2 (2011) 21, https://doi.org/10.4103/2229-5186.79345.
[52] Z. Földhazy, A. Arndt, C. Milgrom, A. Finestone, I. Ekenman, O. Surgeon, Exercise-induceD Strain and Strain Rate in the Distal Radius (86) (2005). ⟨https://doi.org/10.1302/0301-620X.87B2⟩.
[53] A.M. Wessendorf, D.J. Newman, Dynamic understanding of human-skin movement and strain-field analysis, IEEE Trans. Biomed. Eng. 59 (2012) 3432–3438, https://doi.org/10.1109/TBME.2012.2215859.
[54] A.J. Gallagher, A.N. Anniadh, K. Bruyere, M. Otténio, H. Xie, M.D. Gilchrist, Dynamic Tensile Properties of Human Skin, n.d.
[55] B.L. Proffen, M. McElfresh, B.C. Fleming, M.M. Murray, A comparative anatomical study of the human knee and six animal species, Knee 19 (2012) 493–499, https://doi.org/10.1016/j.knee.2011.07.005.